Acoustic Localisation of Chafer Beetle Larvae

Tiger Yotsawat Tawantalerngrit
NST: Part III Physics
University of Cambridge
Supervisor: Dr Christopher Lester

April 13, 2025

Abstract

Understanding how soil parameters will affect range of detection (to determine in what environment detection can be made - guide future designs) Developed and tested device that can be used to test acoustic properties of soil First tested in air: measured speed of sound and attenuation coefficient Results of simulation and agreement with Biot theory or attenuation equation

Contents

1 Introduction

Lawns require regular attention and are often susceptible to damage caused by pests residing beneath the turf. Among the most common lawn pests in the UK are the chafer beetle grubs [3]. The adult stage of the beetle is not a threat to the lawn but their root-feeding larvae eat away at the roots of the grass, resulting in dead patches which can be peeled away from the soil surface [34].

Biological control via the introduction of a certain species of pathological nematodes known as heterorhabditis bacteriophora is the most commonly used method for treating lawns infested with chafer grubs. Other forms of control such as the use of pesticides are not currently approved for use by home gardeners [8]. In general, both biological and chemical methods are used to control pests in lawns and gardens though the former raises concerns due to the question of its host specificity and therefore its ecological impact [27] while the latter due to its toxicity and environmental factors [9].

Physical control methods have the potential to be both environmentally friendly and species specific. However, the prospect of using physical pest control is hindered by the lack of a sensitive and affordable method for locating and distinguishing between pest and non-pest species [36].

An abundance of literature exists on acoustic detection methods including the use of sensitive accelerometers, electret microphones and laser doppler vibrometers to detect insects in grains, wood and plant bodies [26, 29, 21]. It has been found that many species of insects communicate via a process known as stridulation [16]. Vibrations with a species-specific acoustic profile are generated by rubbing together body parts and these propagate through various media such as air, plant stems and soil. This gives a premise for using temporal patterns to distinguish between pest and non-pest activities [25].

In soil, notable work involved using a steel stake inserted into soil at the sampling site. The stake acts as a waveguide coupling vibrations to a sensor attached to its free end [19]. The signal is then amplified and processed using bespoke software, DAVIS [24], to determine the likelihood of site infestation. Subterranean insects produce brief broadband vibrational impulses as a result of their movement and feeding. It was shown that these bursts of impulses have a distinct spectral profile from wind and traffic noise [32]. The feasibilities of mapping out infestation sites and estimating the population density of grubs were shown using these techniques [6, 23].

It is recognised that the high attenuation of sound in soil limits the precision of acoustic measurements [25] but few quantitative models currently exist for how soil conditions affect attenuation. In this report, the three-component model for unsaturated porous media as proposed by Detmann [11] is used as a basis for incorporating the effects of measurable soil properties on wave

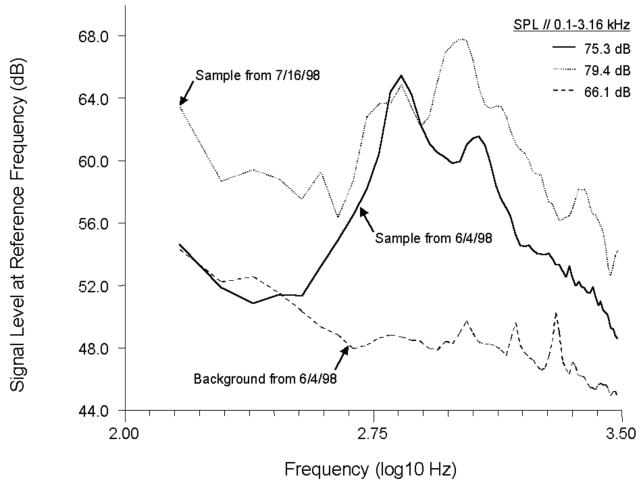

Figure 1: Comparison of chafer beetle acoustic spectrum and quiet background. Adapted from Mankin et al. [25]

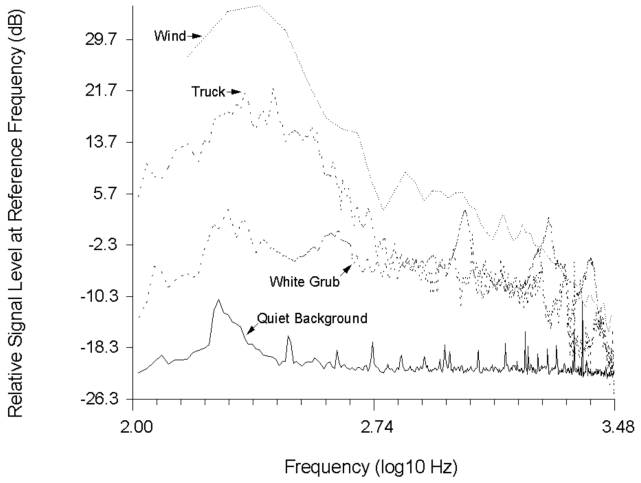

Figure 2: Comparison of chafer beetle acoustic spectrum, vehicle noise and wind noise. Adapted from Mankin et al. [25]

propagation in soil. Through numerical simulation, I outline the soil conditions under which acoustic detection methods are useful. It will be apparent that the effects of soil porosity cannot be deduced from the current model and therefore I propose an experimental setup that allows for the investigation of the dependence of attenuation on porosity.

2 Background

2.1 Chafer Beetle

The European Chafer (Amphimallon majale) is a beetle belonging to the Scarabaeidae family. The white grubs of these beetles feed on grass roots causing extensive damage to lawns and can be visually identified by dead yellow patches of grass. The damage is exacerbated by the fact that their natural predators such as crows, foxes and racoons dig up the loosened patches in search of the grubs. Work by Mankin et al. lays the foundation for the acoustic detection of soil-dwelling insects such as the chafer grubs by providing spectral comparisons between the sounds produced by different species of insects. These acoustic profiles were also shown to be distinguishable from that of other sources of background noise in the field such as wind and traffic noise, both in the time and frequency domain [25].

Figure 1 shows that seismic background noise recorded in the field has a much lower amplitude than the signal of interest at higher frequencies (1/f pink noise?). Figure 2 compares the louder background noise from wind and vehicles with that of the white grubs. Here, the spectral profile of the background noise is broadband and therefore has significant contributions even in the higher frequency region. It can be noted however that there is a much more prominent drop in power at frequencies above 400 Hz compared to that below this frequency. By comparing this power ratio of each spectrum, the background noise can still be distinguished from the insect noise.

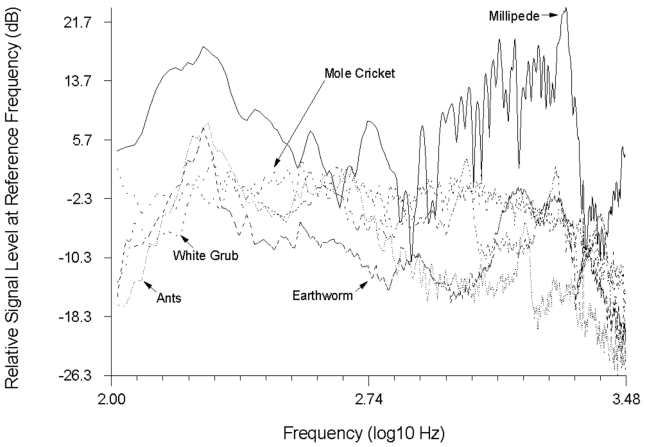

Figure 3: Comparison of insect spectra. Adapted from Mankin et al. [25]

In Figure 3, the Fourier spectra of different species of insects were compared. Each of these spectra are broadband between 0.1 kHz to 3.16 kHz and therefore cannot be reliably distinguished from each other. The broadband feature suggests that the detected sounds are not species-specific stridulations used for communication but rather are produced through movements against the soil and through feeding processes [25]. This, however, does not rule out the possibility of using acoustic signals to selectively detect lawn pests. Once located, further recording can be made at the site of infestation and the time domain signals can be used to listen for the quieter stridulations. Trained listeners are able to distinguish different insect sounds by ear [24].

2.2 Soil Physics

Soil is a porous medium through which water, gas and solutes can move. The solid skeleton of soil is typically composed of sedimentary materials such as sandstone, peat soil, granular soil, clay or limestone depending on the soil type. In naturally occurring soil samples, the pore space between the solid grains is in general filled with at least two immiscible fluids, namely air and water, unless the soil is saturated in which case the entire pore space is occupied by water. Topsoil is the uppermost layer of soil, typically the top 30 cm from the surface, with the highest concentration of microorganisms and is therefore the layer of interest in this study [4]. In modelling the soil, the two quantities of interest are porosity and saturation. These can be readily determined in the field and exhibit seasonal variation [7]. The temporal variation of these quantities would affect the attenuation of sound waves and hence the acoustic detectability of the chafer beetle grubs are highly dependent on soil conditions. As acoustic waves in soil also propagate through the pore fluids, the concepts of capillary pressure and permeability are also introduced at this point.

2.2.1 Porosity

Porosity is a measure of how tightly packed the soil is. It is defined as the ratio of volume of void, either filled by a single pore fluid or a mixture of immiscible fluids, to the entire representative volume element (RVE). The RVE is a concept in continuum mechanics that allows heterogeneous materials to be modelled as a continuous body [18]. The RVE is defined as the volume that effectively includes a sampling of all microscopic heterogeneity and yet remains small enough to be considered a volume element.

$$n = \frac{V_{\varnothing}}{V_{RVE}} \tag{1}$$

where $V_{\varnothing}$ is the volume of void within the RVE and V_{RVE} is the volume of the RVE.

2.2.2 Saturation

As the aim is to model unsaturated soil samples, one needs to introduce another microstructural variable known as the degree of saturation. This is defined as the ratio of the volume of a single phase of pore fluid over the entire volume of void within an RVE. The sum of the degree of saturations over all fluid types is by definition equal to one.

$$S^{\theta} = \frac{V^{\theta}}{V_{RVE}} \quad \text{where } \theta \in \{F, G\} \tag{2}$$

where the subscript indices F and G denote variables relating to water and air respectively. From this point onwards, as we are dealing only with water and air as our two pore fluids, we shall drop the theta suffix and define the degree of saturation for water as S and therefore it follows that the degree of saturation for air is $1 - S$.

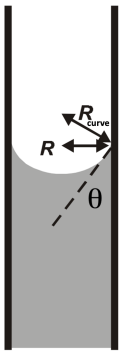

Figure 4: Capillary angle. Adapted from Glover. [15]

2.2.3 Capillary Pressure

Capillary pressure is the pressure that exists at the interface between two immiscible fluids in a thin tube, or in this case the narrow pore spaces between the solid skeleton. The fluid with the higher wettability—the tendency to be adsorbed by the capillary walls—is defined as the wetting phase while the other is defined as the non-wetting phase. In the case of a water-air mixture in sandstone, water is the wetting phase. We define capillary pressure as the pressure difference at the interface of the fluids

$$p_c = p_{non-wetting} - p_{wetting} \tag{3}$$

This quantity is important as it is the main driving force responsible for the third type of compressional wave $P3$ that arises in unsaturated porous media [11].

Although pore spaces in soil has a rather complex geometry, if we approximate these as bundles of capillary tubes, we get that the capillary pressure is related to surface tension γ by

$$p_c = \frac{2\gamma}{R_{curve}}, \tag{4}$$

where R_{curve} is the radius of curvature of the fluid meniscus, γ is the surface tension at the wetting-non-wetting interface. As seen in Figure 4 if we let R by the radius of the capillary tube then we see that $R_{curve} = R/\cos\theta$ where θ is the wetting angle which is a constant determined by the balance of surface energy between each material phase. The contact angle is given by Young's equation [5]:

$$\cos\theta = \frac{\gamma^{SG} - \gamma^{SF}}{\gamma^{FG}} \tag{5}$$

From Equation 4, we see that the capillary pressure p_c must depend on the surface energy γ, which for a given mixture of pore fluid is a constant, and importantly the pore radius. Relating this to the soil property,

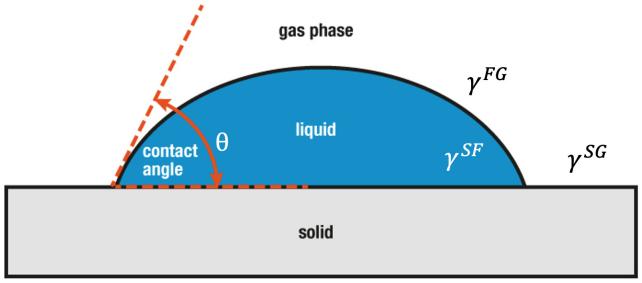

Figure 5: Wetting angle. Adapted from Bai and Wen [5]

the greater the porosity, the larger the pore radius and hence the smaller the capillary pressure.

If a wetting fluid is introduced at one end of a soil sample saturated by a non-wetting phase, the wetting fluid is spontaneously drawn in by the capillary pressure in a process known as imbibition. An analogue of this is when a non-wetting fluid is introduced to the sample saturated by a wetting fluid. In this case, the process is called drainage and a displacement pressure is required to overcome the capillary force holding the fluid in place [15].

By considering this drainage process and modelling the pores as bundles of capillary tubes, it is possible to deduce that capillary pressure should increase as water saturation decreases in the soil sample. This is because capillary pressure is inversely proportional to the radius of the tube in our simple model. Initially, as air is introduced into the water-saturated soil sample, a relatively small displacement pressure is needed to displace water from larger pores. As these pores are filled by the air, an increasingly large pressure is needed to further displace the water from smaller pores. Later a relation between capillary pressure and saturation proposed by van Genuchten to fit experimental data for the air-water-sandstone mixture will be used for some numerical examples.

2.2.4 Permeability

The permeability parameter k measures how well a porous medium can transmit fluid. It is related to the hydraulic conductivity K which is a parameter used to describe how easily a certain fluid flows through a particular porous media by

$$k = \frac{K\eta}{\rho g}, \tag{6}$$

where η and ρ are the viscosity and density of the fluid, and g is the acceleration of free fall [37]. While K is dependent on the properties of the fluid, k is a property of the porous material only. K is defined by Darcy's law [22], the porous media analogue to Ohm's law for electrical circuits.

$$\frac{Q}{A} = -K\frac{dh}{dl}, \tag{7}$$

where Q is the volumetric flow rate, A is the cross-sectional area through which the fluid flows and dh/dl is the hydraulic gradient. In defining the hydraulic gradient, the concept of hydraulic head must be introduced. The hydraulic head h has units of length and represents the energy per unit weight of the pore fluid due to its elevation and pore pressure [17]. The hydraulic gradient dh/dl is the change in head per unit distance along the direction of greatest change in head. That is to say that fluid flows in the direction of maximum decrease in hydraulic head.

2.3 Towards A Three-Component Model

In this section, we aim to build towards a description of unsaturated soil as a three-component poroelastic medium [13]. To do this, we first introduce the balance laws [20], presented in the Eulerian picture, for the simpler problem of fluid saturated soil. These arise in the discussion of the classical models used to describe porous media under the framework of continuum mechanics. Continuum mechanics allows us to view the material as a continuous mass rather than as discrete particles [31] through the use of a representative volume element (RVE) defined in Section 2.2.1. The models that will be discussed are the Full Model, Biot's Model and the Simple Mixture Model. The latter two models can be obtained from the Full Model by making a series of simplifying assumptions [12].

From these models, saturated porous media are shown to support three types of waves—one shear wave S and two compressional waves, $P1$ and $P2$. The S and $P1$ waves are attributed to the solid skeleton while the $P1$ wave is due to the pore fluid. The three-component model extends these by allowing for the existence of a second fluid immiscible with the first. It was shown that a third type of wave, $P3$, emerges due to the capillary pressure between the two fluids. In practice, both $P2$ and $P3$ waves are difficult to measure experimentally as they are heavily attenuated.

2.3.1 Full Model

The Full Model considers a two-component mixture of a solid skeleton S and a single pore fluid F. The model then defines a set of fields, rhotheta for the partial densities, vtheta for the velocities and n for the porosity where the superscript $\theta \in \{S, F\}$ where S and F denote the solid and fluid phases respectively. These fields must then satisfy the balance laws. The balance laws capture the idea that the rate of change of a quantity within a volume must be due to one or more of the following—the flow of the quantity through the surface that bounds the volume, a source that is on the boundary and a source that is within the volume itself [20]. For the fields mentioned then [39],

- partial mass balance equations

$$\frac{\partial \rho^\theta}{\partial t} + \rho_0^\theta \operatorname{div} \mathbf{v}^\theta = 0 \quad \text{where } \theta \in \{S, F\} \tag{8}$$

- partial momentum balance equations

$$\rho_0^\theta \frac{\partial \mathbf{v}^\theta}{\partial t} = \operatorname{div} \mathbf{T}^\theta + \hat{\mathbf{p}}^\theta \quad \text{where } \theta \in \{S, F\} \tag{9}$$

- porosity balance equation

$$\frac{\partial \Delta n}{\partial t} + \phi \operatorname{div} (\mathbf{v}^{\mathrm{F}} - \mathbf{v}^{\mathrm{S}}) = \hat{\mathrm{n}}, \quad \Delta \mathrm{n} = \mathrm{n} - \mathrm{n}_{\mathrm{eqm}} \tag{10}$$

By defining extra constitutive relations for the Cauchy Tensors, the momentum source and the porosity source, the evolution of the set of fields is determined. A more detailed treatment of the Full Model can be found in Wilmanski's work [39].

The Full Model is, in practice, difficult to apply. Certain simplifications can be made depending on the application. The Biot's Model is the most frequently used model to describe processes in fluid-saturated porous media. It can be shown that the Full Model is identical to Biot's Model provided that the porosity gradient goes to zero. The Simple Mixture Model follows further from the Biot's model if we neglect the coupling constant between the fluid and the solid phases, the off-diagonal terms in the density matrix and finally the viscosity effects by assuming that the permeability parameter is independent of frequency.

2.3.2 Three Component Model

Extending the same ideas as those introduced in the Full Model but this time adding the contributions of a second pore fluid and making some linearising approximations, we arrive at the Three-Component Model as shown by Wilmanski [39]. The set of unknown fields to be solved for are

$$\{\rho^\theta, \mathbf{v}^\theta, \mathbf{e}^S, n\} \quad \text{where } \theta \in \{S, F, G\} \tag{11}$$

where ρ^θ are the partial densities, $\mathbf{v}^\theta$ are the velocities, $\mathbf{e}^S$ is the macroscopic deformation tensor for the skeleton and n denotes the porosity. To be able to linearise the model, the following conditions must be true:

$$\max\{||\mathbf{e}^S||, |\epsilon^F|, |\epsilon^G|, |\frac{n - n_0}{n_0}|, |\frac{S - S_0}{S_0}|\} << 1 \tag{12}$$

$$\text{where } ||\mathbf{e}^S \equiv max\{|\lambda_e^{(1)}|, |\lambda_e^{(2)}|, |\lambda_e^{(3)}|\}, \tag{13}$$

$$\epsilon^F \equiv \frac{\rho_0^F - \rho^F}{\rho_0^F}, \quad \epsilon^G \equiv \frac{\rho_0^G - \rho^G}{\rho_0^G} \tag{14}$$

(i.e. the deviations from equilibrium are small)

where the subscript zero's denote the initial value of each quantity, lambdas are the eigenvalues of the deformation tensor eS and F, G are the volume changes of the two fluid phases. The balance laws are similar to the full model but now with the additional balance equations for the second pore fluid. To distinguish between the two fluids, let us denote the parameters corresponding to the wetting phase and non-wetting phase with superscripts F and G respectively.

- conservation of mass

$$\frac{\partial \rho^\theta}{\partial t} + \rho_0^\theta \operatorname{div} \mathbf{v}^\theta = 0 \quad \text{where } \theta \in \{S, F, G\} \tag{15}$$

- balance of linear momentum

$$\rho_0^\theta \frac{\partial \mathbf{v}^\theta}{\partial t} = \operatorname{div} \mathbf{T}^\theta + \hat{\mathbf{p}}^\theta \quad \text{where } \theta \in \{S, F, G\} \tag{16}$$

- porosity balance equation

$$\frac{\partial \Delta n}{\partial t} + \phi \operatorname{div} \mathbf{J} = \hat{\mathrm{n}}, \quad \Delta \mathrm{n} = \mathrm{n} - \mathrm{n}_{\mathrm{eqm}} \tag{17}$$

The constitutive relations for the stress tensors are:

$$\mathbf{T}^S = \mathbf{T}_0^S + \lambda^S e \mathbf{1} + 2\mu^S \mathbf{e}^S + Q^F \epsilon^F \mathbf{1} + Q^G \epsilon^G \mathbf{1}, \quad e \equiv \operatorname{tr} \mathbf{e}^S \tag{18}$$

$$\mathbf{T}^F = -p^F \mathbf{1}, p^F = p_0^F - p_0^F \kappa^F \epsilon^F - Q^F e - Q^{FG} \epsilon^G \tag{19}$$

$$\mathbf{T}^G = -p^G \mathbf{1}, p^G = p_0^G - p_0^G \kappa^G \epsilon^G - Q^G e - Q^{FG} \epsilon^F \tag{20}$$

The linear constitutive relations for the flux of porosity and for the momentum sources are given by:

$$\hat{\mathbf{p}}^S = \pi^{FS}(\mathbf{v}^F - \mathbf{v}^S) + \pi^{GS}(\mathbf{v}^F - \mathbf{v}^S) \tag{21}$$

$$\hat{\mathbf{p}}^F = -\pi^{FS}(\mathbf{v}^F - \mathbf{v}^S), \quad \hat{\mathbf{p}}^G = -\pi^{GS}(\mathbf{v}^G - \mathbf{v}^S) \tag{22}$$

$$\hat{n} = -\frac{n - n_e qm}{\tau_n}, \quad n_e qm = n_0(1 + \delta e) \tag{23}$$

$$\mathbf{J} = \phi^F(\mathbf{v}^F - \mathbf{v}^S) + \phi^G(\mathbf{v}^G - \mathbf{v}^S) \tag{24}$$

Finally, solving the balance equations and representing the partial densities instead by volume changes of the components, we end up with the following field equations for the new set of fields $\{\mathbf{v}^\theta, \mathbf{e}^S, \epsilon^F, \epsilon^G, n\}$ where $\theta \in \{S, F, G\}$ [11]:

$$\rho_0^S \frac{\partial \mathbf{v}^S}{\partial t} = \operatorname{div}\{\lambda^S e\mathbf{1} + 2\mu^S \mathbf{e}^S + Q^F \epsilon^F \mathbf{1} + Q^G \epsilon^G \mathbf{1}\} \tag{25}$$

$$+ \pi^{FS}(\mathbf{v}^F - \mathbf{v}^S) + \pi^{GS}(\mathbf{v}^F - \mathbf{v}^S), \tag{26}$$

$$\rho_0^F \frac{\partial \mathbf{v}^F}{\partial t} = \operatorname{grad}\{\rho_0^F \kappa^F \epsilon^F + Q^F e + Q^{FG} \epsilon^G \tag{27}$$

$$- \pi^{FS}(\mathbf{v}^F - \mathbf{v}^S)\}, \tag{28}$$

$$\rho_0^G \frac{\partial \mathbf{v}^G}{\partial t} = \operatorname{grad}\{\rho_0^G \kappa^G \epsilon^G + Q^G e + Q^{FG} \epsilon^F \tag{29}$$

$$- \pi^{GS}(\mathbf{v}^G - \mathbf{v}^S)\}, \tag{30}$$

$$\frac{\partial \mathbf{e}^S}{\partial t} = \operatorname{sym}\operatorname{grad}\mathbf{v}^S, \tag{31}$$

$$\frac{\partial \epsilon^F}{\partial t} = \operatorname{div}\mathbf{v}^F, \quad \frac{\partial \epsilon^G}{\partial t} = \operatorname{div}\mathbf{v}^G, \quad e \equiv \operatorname{tr}\mathbf{e}^S \tag{32}$$

$$n = n_0 \left[1 + \delta e + \frac{\phi^F}{n_0}(e - \epsilon^F) + \frac{\phi^G}{n_0}(e - \epsilon^G)\right] \tag{33}$$

2.4 Wave Propagation

Wave analysis is done by assuming the following wave ansatz for the essential fields [10]:

$$\mathbf{e}^S = \mathbf{E}^S \psi, \quad \epsilon^F = E^F \psi, \quad \epsilon^G = E^G \psi, \tag{34}$$

$$\mathbf{v}^\theta = \mathbf{V}^\theta \psi \quad \text{where } \theta \in \{S, F, G\}, \tag{35}$$

$$n - n_0 = D\psi, \quad \psi \equiv \exp i(\mathbf{k}\cdot\mathbf{x} - \omega t) \tag{36}$$

where $\mathbf{E}^S$, $E^{\{F,G\}}$, $\mathbf{V}^{\{S,F,G\}}$ and D have constant amplitudes, ω is a given frequency and $\mathbf{k} = k\mathbf{n}$ is a wave vector with $\mathbf{n}$ being the unit vector in the direction of propagation. The dispersion relations that follow are split into the transverse case and the longitudinal case.

Transverse:

$$\omega^2\big[1 - \frac{\mu^S}{\rho_0^S}\big(\frac{k}{w}\big)^2\big] - \pi^{FS}\pi^{GS}\frac{\rho_0^S + \rho_0^F + \rho_0^G}{\rho_0^S\rho_0^F\rho_0^G}$$
$$\times\big[1 - \frac{\mu^S}{\rho_0^S + \rho_0^F + \rho_0^G}\big(\frac{k}{w}\big)^2\big] + i\omega\big\{\frac{\pi^{FS} + \pi^{GS}}{\rho_0^S}$$
$$+ \big(\frac{\pi^{FS}}{\rho_0^F} + \frac{\pi^{GS}}{\rho_0^G}\big)\big[1 - \frac{\mu^S}{\rho_0^S}\big(\frac{k}{w}\big)^2\big]\big\} = 0$$

Longitudinal:

$$\sum_{m=0}^{2} A_m(\omega)\left(\frac{k}{\omega}\right)^{2m} = 0 \tag{37}$$

where the complex coefficients $A_m(\omega)$ are given by:

$$A_0(\omega) = \omega^2 - \pi^{FS}\pi^{GS}\frac{\rho_0^S + \rho_0^F + \rho_0^G}{\rho_0^S\rho_0^F\rho_0^G}$$
$$+ i\omega\big(\frac{\pi^{FS} + \pi^{GS}}{\rho_0^S} + \frac{\pi^{FS}}{\rho_0^F} + \frac{\pi^{GS}}{\rho_0^G}\big)$$
$$A_1(\omega) = \omega^2\big(\frac{\lambda^S + 2\mu^S}{\rho_0^S} + \kappa^F + \kappa^G\big)$$
$$+ \frac{\lambda^S + 2\mu^S}{\rho_0^S}\frac{\pi^{FS}\pi^{GS}}{\rho_0^F\rho_0^G} + \frac{\pi^{FS}\pi^{GS}}{\rho_0^S\rho_0^F\rho_0^G}[\rho_0^F\kappa^F + \rho_0^G\kappa^G$$
$$+ 2(Q^F + Q^G + Q^{FG})]$$
$$- i\omega\big[\frac{\lambda^S + 2\mu^S}{\rho_0^S}\big(\frac{\kappa^F}{\rho_0^F} + \frac{\kappa^G}{\rho_0^G}\big)$$
$$+ \frac{(\pi^{FS} + \pi^{GS})(\kappa^F + \kappa^G)}{\rho_0^S}$$
$$+ \frac{\pi^{FS}\kappa^G + \pi^{GS}\kappa^F}{\rho_0^F} + 2\frac{\pi^{FS}Q^F}{\rho_0^S\rho_0^F} + 2\frac{\pi^{GS}Q^G}{\rho_0^S\rho_0^G}\big]$$
$$A_2(\omega) = \omega^2\big[\frac{\lambda^S + 2\mu^S}{\rho_0^S}(\kappa^F + \kappa^G) + \kappa^F\kappa^G$$
$$- \frac{\rho_0^S Q^{FG^2} + \rho_0^F Q^{G^2} + \rho_0^G Q^{F^2}}{\rho_0^S\rho_0^F\rho_0^G}\big]$$
$$+ i\omega\big[\frac{\lambda^S + 2\mu^S}{\rho_0^S}\big(\frac{\pi^{FS}\kappa^G}{\rho_0^F} + \frac{\pi^{GS}\kappa^F}{\rho_0^G}\big)$$
$$+ \frac{(\pi^{FS} + \pi^{GS})\kappa^F\kappa^G}{\rho_0^S}$$
$$- \frac{\pi^{FS}}{\rho_0^S\rho_0^F\rho_0^G}(Q^G + Q^{FG})^2 - \frac{\pi^{GS}}{\rho_0^S\rho_0^F\rho_0^G}(Q^F + Q^{FG})^2$$
$$+ 2\frac{\pi^{GS}\kappa^F Q^G}{\rho_0^S\rho_0^G} + 2\frac{\pi^{FS}\kappa^G Q^F}{\rho_0^S\rho_0^F}\big]$$
$$A_3(\omega) = \omega^2\big[\frac{\lambda^S + 2\mu^S}{\rho_0^S}\big(\frac{Q^{FG^2}}{\rho_0^F\rho_0^G} - \kappa^F\kappa^G\big)$$
$$+ \frac{Q^{F^2}\kappa^G}{\rho_0^S\rho_0^F} + \frac{Q^{G^2}\kappa^F}{\rho_0^S\rho_0^G}\big]$$
$$- 2\frac{Q^F Q^G Q^{FG}}{\rho_0^S\rho_0^F\rho_0^G}$$

The partial densities are simply related to the real densities of the pure material by: $\rho^S = n\rho^{SR}$, $\rho^F = nS\rho^{FR}$, $\rho^G = n(1-S)\rho^{GR}$ A set of material parameters $\{\lambda^S + (2/3)\mu^S, F, G, Q^F, Q^G, Q^{FG}\}$ appears in the dispersion relations which are dependent on the initial porosity and saturation of the soil. This allows us to investigate the dependence of the wave velocity and attenuation on the soil conditions. λ^S and μ^S are the first and second Lamé constants for the solid grains respectively. The latter is also equivalent to the shear modulus. F and G are the compressibility factor of the two fluids defined as $\kappa = PV_m/RT$ where P is the pressure, V_m is the molar volume, R is the universal gas constant and T is the temperature [28]. By definition, the compressibility factor of an ideal gas is unity. Finally Q^F, Q^G and Q^{FG} are the solid-wetting, solid-non-wetting and

wetting-non-wetting coupling constants respectively.

3 Numerical Simulation

The dispersion relations obtained in the previous section can be solved for the complex wavenumber. The wave velocity and attenuation coefficient can be calculated from the complex wavenumber $\mathbf{k}$ as follows:

$$v = \frac{\omega}{|real(\mathbf{k})|} \tag{38}$$

$$\alpha = |im(\mathbf{k})| \tag{39}$$

where v is the phase speed and α is the attenuation coefficient.

In this section, numerical results for a particular sandstone-water-gas mixture are presented. The phase speed and attenuation coefficient of the acoustic waves are plotted against soil saturation and also against frequency.

Prior to obtaining numerical results for the wavenumber, there are parameters in the dispersion relations that are yet undefined. These are the set of material parameters $\{\lambda^S + (2/3)\mu^S, F, G, Q^F, Q^G, Q^{FG}\}$. Following the approach used by Detmann [10], these macroscopic material parameters can be derived from a set of microscopic parameters that are dependent on the microstructure of the bulk material. This is done by borrowing the relations from Santos, Corbero and Douglas [33]. In Santos et al.'s approach, the set of material parameters $K_c^*, B_1, B_2, M_1, M_2, M_3$ that were used are different from those appearing in the dispersion relations. Detman shows, however, that these have a simple relationship with the set of parameters $\{\lambda^S + (2/3)\mu^S, F, G, Q^F, Q^G, Q^{FG}\}$ that we wish to evaluate.

It is important to note here that the capillary pressure implicitly enters the dispersion relation via these parameters. The dependence of capillary pressure on soil saturation can be obtained empirically through experiments or via closed-form equations such as those proposed by Santos et al. or van Genuchten [14]. The former is chosen for this simulation and is shown in Figure 6.

$$p_c = p_{c_r} e^{-AS_{o_r}} \left(e^{-AS_o} - 1\right) \tag{40}$$

where $A = 6.029\,158$, $S_{o_r} = 0.519$, $p_{c_r} = 0.000\,002\,650\,910\,9 \times 10^9$. Calculating Santos et al.'s parameters with the capillary relation above and mapping the results to the Detman material parameters using equations [ref relation] yield a relationship between the material parameters and soil saturation. Figure 7 shows the parameters for the case of a sandstone-water-gas mixture. The sandstone skeleton and the pore fluids have the following properties:

$$n_0 = 0.25,\ \rho_0^{SR} = 2650\,\mathrm{kg\,m^{-3}},\ K^S = 48\,109\,\mathrm{Pa}, \tag{41}$$

$$K^d = \frac{K^S}{1 + g n_0},\ g = 50,\ k = 1 \times 10^{-7}\,\mathrm{m^2} \tag{42}$$

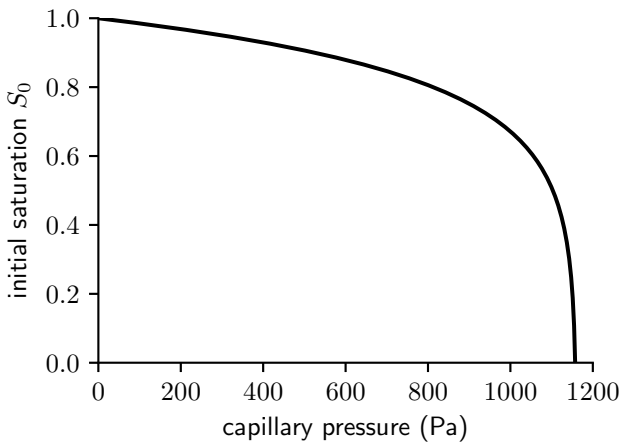

Figure 6: Plot of Santos' capillary pressure

Table 1: caption

	water	gas
$\rho_0^{\theta R}(\mathrm{kg\,m^{-3}})$	1000	100
$K^\theta(\mathrm{Pa})$	2.25×10^9	2.2×10^7
$\mu^\theta(\mathrm{mPa\,s}), 20°\mathrm{C}$	1	0.015

where n_0 is the initial porosity, ρ_0^{SR} is the true density of the material with zero porosity, K^S is the bulk modulus of the grains and K^d is the drained modulus which represents the bulk modulus of the empty matrix. The constant g is a fitting constant that is found by fitting the expression with experimental data obtained from different soil types [38].

Finally, wave propagation also depends on the resistance parameters π. These are related to the permeability parameter (see permeability) by $\pi = \eta/k$ where η is the viscosity of the fluid and k is the permeability parameter for the soil. This describes the resistance of the porous material against the flow of the fluid. It is

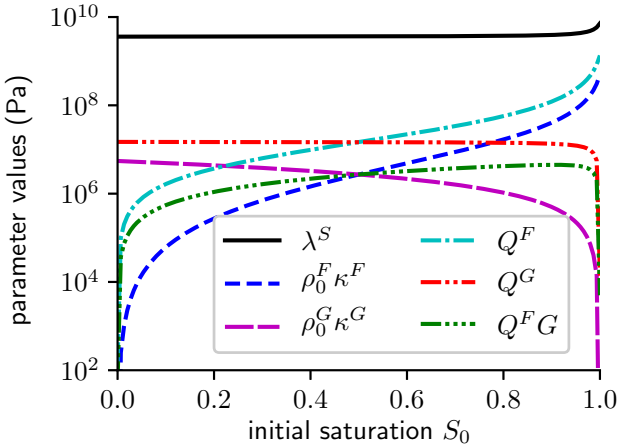

Figure 7: Plot of Detmann's material parameters

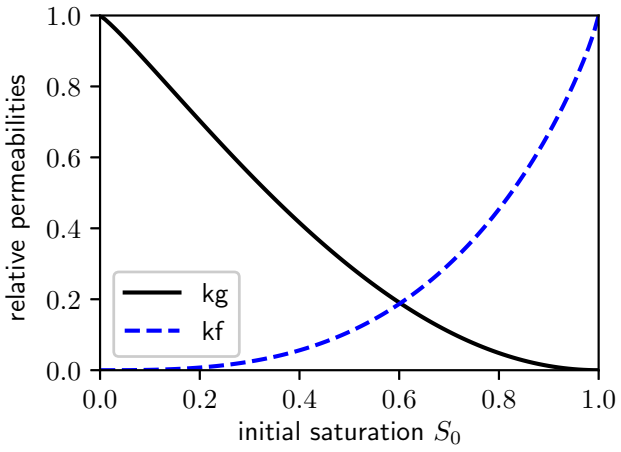

Figure 8: Relative permeabilities

assumed that the resistance parameter for the fluid mixture can be separated into the effective resistance for the water and gas

$$\pi^{FS} = \frac{\pi^F}{k^F} \quad \text{and} \quad \pi^{GS} = \frac{\pi^G}{k^G} \tag{43}$$

where π^{FS} and π^{GS} are the effective resistances, π^F and π^G are the experimentally determined resistance parameters of each fluid. k^F and k^G are the relative permeabilities which depend on saturation. The theoretical relationship as proposed by van Genuchten [14] that fits with experimentally determined behaviour [40] are given by

$$k^F = S^{\frac{1}{2}}\left[1-\left(1-S^{\frac{1}{m}}\right)^m\right]^2 \quad \text{and} \quad k^G = (1-S)^{\frac{1}{3}}\left(1-S^{\frac{1}{m}}\right)^{2m} \tag{44}$$

where $m = 0.85$, a fitting parameter. Figure 8 shows the relative permeabilities plot.

3.1 Velocity, Attenuation and Detection Range

The dispersion relations have been solved for the complex wavenumber k as a function of angular frequency of the wave and soil saturation in the sandstone-water-gas case. In Figure 9, the phase speed and attenuation coefficient are plotted against frequency and in Figure 10 against saturation. The contour plots of saturation against frequency in Fig(ref) shows, for the transverse wave case, the region within the frequency range of interest where detection range is maximal.

3.2 Remarks

I demonstrated in this numerical simulation section that given the material parameters shown in Table 1 and Equations 41, which are measurable quantities of the constituent materials of the soil, and expressions for capillary pressure pc and relative permeabilities, k^F and

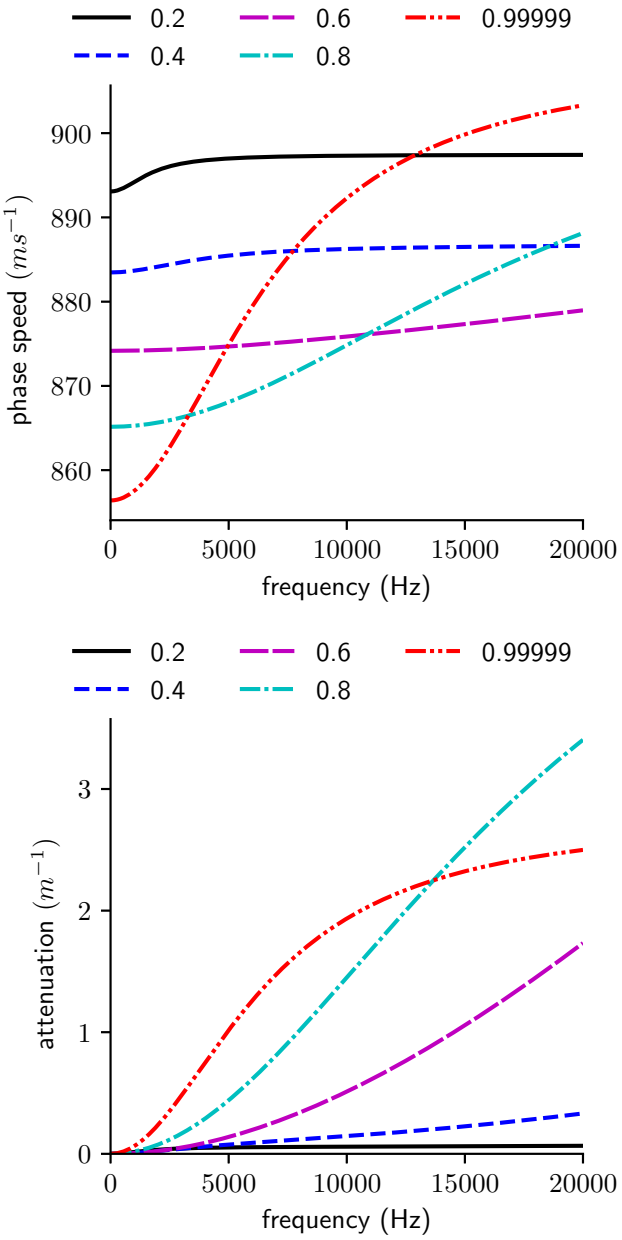

Figure 9: Plot against frequency

k^G, in terms of saturation, it is possible to predict the wave velocity and attenuation coefficients for a given frequency and soil saturation. If the dependence of p_c, k^F and k^G on porosity is also known, it would be possible to have porosity as another independent variable.

Figure 7 shows the behaviour of the material parameters as saturation is varied. The parameter $\lambda^S + (2/3)\mu^S$ is roughly independent of saturation which is expected as this is a property of the solid skeleton and therefore is not influenced by the composition of the pore fluids. The parameters relating to each pore fluid also behave as expected with the sandstone-water coupling constant and the compressibility factor of the water reaching a maximum but finite value when the soil is saturated with water ($S = 1$) and going to zero when there is no water in the pores ($S = 0$). The analogue is true for the parameters relating to the existence of the gas. The coupling constant QFG between the fluids is zero when either one of the fluids disappears and is maximum near intermediate saturation values.

Figures 10 attempt to replicate results from [11]. However, the non-smooth variations at extreme values of frequencies and saturations point towards non-convergence or convergence to the wrong roots for k in the numerical solutions. For intermediate values of saturation and frequencies, the plots are well behaved. It is noted in Detmann's work [10] that limitations to the model exist for very low saturation values. In this low saturation regime, the water can no longer be assumed to be continuous as the structure of the fluid mixture is frothy.

4 Experimental Methods

The aim of the experimental section is to demonstrate the methods that can be used to verify key results from the three-component model and to investigate how the wave speed and attenuation depend on porosity. The latter is not currently predicted by the model.

The experiment had not reached a stage suitable for soil testing at the time of the Covid-19 lockdown and therefore the soil preparation methods are included below as experimental plans in the interest of completeness. Soil Preparation In Cambridge, the soil composition is a mixture of freely draining lime-rich loamy soil and lime-rich clayey soil with impeded draining [1, 35]. The soil selected is loamy clay soil commonly used for lawn preparation, representative of that found in the area.

The process of soil preparation will involve sifting, compacting and watering. The soil sample will be prepared by passing the sample through a sieve to exclude large materials $> 4\,\text{mm}$. To avoid having to air-dry the sample for one week prior to introducing known volume of water, as often done in literature [30], the saturation of the soil can be determined through a method based on water extraction as will be described in detail. To vary porosity and saturation, an arbitrary volume of water is added to the sieved sample and an arbitrary compacting force is applied.

Measurement of the microstructural variables—namely porosity and saturation—will be done by excavating two samples of soil immediately after acoustic measurements are performed. One sample undergoes the porosity measurement while the other is measured for water content.

A crude experimental method to determine porosity is by saturating the soil by adding water until the water level just reaches the soil surface. Using this method, there will be residual air [2] in the pores due to excess atmospheric pressure (see Capillary pressure). The small error introduced by this residual pressure does not limit precision of the experiment. The mass of the saturated sample is recorded. The sample is then dried on a hot plate, again leaving residual water in the pores held by capillary pressure. The dry mass is measured. Since the density of water is a known quantity, the pore space is related to the change in mass by $n = (\text{saturated mass} - \text{dry mass})/\rho^F$.

Saturation is determined in a similar fashion but this time by subtracting the dry mass instead from the initial mass of the wet but unsaturated soil. $n = (\text{unsaturated mass} - \text{dry mass})/\rho^F$. Source and Detector Calibration (control voltage-freq, freq-freq, freq-amplitude) Why chose electret microphone for detector [24] Why piezoelectric speaker Producing the bass Chosen to omit the steel stakes because want direct coupling between the detector and the Signal Processing Amplification, Bandpass Filter, Differential Op-Amp Velocity and Attenuation Velocity determined using phase shift between input signal and measured signal Phase shift = kx - wt + extra constant phase shift introduced by circuit and components If we just plot phase shift against the relative distance between speaker and microphone then k just the gradient Velocity is then v = w/k Attenuation can be determined by plotting x against log(amplitude) where the voltage output measured from the microphone is directly proportional to the pressure of the sound wave (ref datasheet for microphone) Note on attenuation: effects of reflection and diffraction Noise Twisting wires - so that they trace the same path in space and so effects from the external EM field would affect each wire equally and so does not affect measured potential difference. Isolating circuits Decoupling capacitors Possible reflections from walls and objects nearby Results Calibration A control voltage was input into the function generator to electronically control the frequency of the speaker. Below the control voltage from the user interface is plotted against the measured voltage input to the function generator (fig 10). Figure 11 shows the frequency measured vs the control voltage. We see that the setup can achieve a frequency range between 4 - 12 kHz which is more than enough for our range of interest.

Fig 10.

Fig 11.

Speed of Sound in Air A trial measurement was done in air to see if the setup works We know the expected

result for speed of sound in air so this would be a sensible sanity check

Fig 12. The phase speed was calculated from this plot. The wavenumber k is the gradient of the line. Frequency used was 1515 Hz giving speed 344 +- errors $ms^{-}1$.

The measured amplitude is plotted against relative distance between the speaker and the microphone. We expected an exponential decay but as can be seen in figure 13 and 14, there are other effects that come into play. These could be due to diffraction or dispersion of the sound wave (since the sound wave is not a plane wave). With the current data, it would not be possible to calculate the attenuation coefficient

Off-axis case

Fig 13. On-axis case

Fig 14. Discussion Comment on reliability of source and detector system - sensitivity, noise to signal ratio, frequency range where response is linear Extended source hypothesis - the non-exponential nature in Fig 13 and 14 might be due to the fact that the speaker is not a plane wave source Conclusion Reflection on COVID-19 Future Direction of experiment Trying with steel stake as waveguides, coupling vibration from soil to detector attached to stake (see how that improves range - in our case, got really good signal to noise ratio anyways) Introduce noise (wind, trucks) Algorithm to detect signal by considering the fact that insect sounds come in short bursts as opposed to constant wind noise and also the frequency spectrum of wind and vehicles drops more sharply for f ¿ 400 Hz Multiple sources and triangulation (ref triangulation) Possible improvements, assumptions to test Thing with potential divider problem when connecting to input sweep Choosing how much the signal is amplified by Circuit board not completely independent (electrical noise) Results summary Numerical result shows sensible behaviour predicted by the three-component model The attenuation coefficient predicted by the model agrees with experimental findings: S and P1 waves not significantly attenuated so can be detected while P2 and P3 waves are difficult to detect in experiments Model predicts what happens to the attenuation and speed of plane acoustic waves in soil if saturation and frequency is varied but not enough information is available to predict dependence on porosity. Learned many things setting up the experiment especially debugging electrical circuits and signal processing The experiment which was meant to verify attenuation and phase speed relationships did not end up working for attenuation measurements but was able to measure wave speed quite easily using phase difference between the wave emitted at the speaker and that detected at the microphone More work needs to be done to understand why the attenuation curve does not display the usual exponential decay References Appendix Calibration Derivation of equations Electrical component values Python code

References

[1] 2004. URL: http://www.landis.org.uk/soilscapes/.

[2] M. Adamski, V. Kremesec, and R. J. Charbeneau. "Residual Saturation: What is It? How is It Measured? How Should We Use It?" In: *J. Environ. Sci.* (2005).

[3] D. V. Alford. "Insects". In: *Pests of Ornamental Trees, Shrubs and Flowers: A Color Handbook*. Second. Elsevier Academic Press, 2012, pp. 20–404.

[4] D. Arrouays, W. Deslais, and V. Badeau. "The Carbon Content of Topsoil and Its Geographical Distribution in France". In: *Soil Use Manage.* 17.1 (2006), pp. 7–11. DOI: 10.1111/j.1475-2743.2001.tb00002.x.

[5] S. Bai and S. Wen. "Vapor-condensed Gas Lubrication of Face Seals". In: *Gas Thermohydrodynamic Lubrication and Seals*. Academic Press, 2019, pp. 143–165.

[6] J. L. Brandhorst-Hubbard et al. "Mapping of Soil Insect Infestations Sampled by Excavation and Acoustic Methods". In: *J. Econ. Entomol.* 94.6 (2001), pp. 1452–1458. DOI: 10.1603/0022-0493-94.6.1452.

[7] M. G. Castiglioni et al. "Seasonal Variation of Soil Aggregate Stability, Porosity and Infiltration During a Crop Sequence Under No Tillage". In: *Revista Terra Latinoamericana* 36.3 (2018). DOI: 10.28940/terra.v36i3.333.

[8] *Chafer Grubs in Lawns*. URL: https://www.rhs.org.uk/advice/profile?pid=487.

[9] L. Crampton. *Biological vs. Chemical Pest Control: Benefits and Disadvantages*. Mar. 2020. URL: https://owlcation.com/agriculture/Biological-vs-Chemical-Pest-Control.

[10] B. Detmann. "Analysis of the Propagation of Sound Waves in Partially Saturated Soils by Means of a Macroscopic Linear Poroelastic Model". In: *Transport in Porous Media* 80.1 (2009), pp. 173–192. DOI: 10.1007/s11242-009-9360-y.

[11] B. Detmann. "Modeling And Numerical Analysis Of Wave Propagation In Partially Saturated Porous Media". In: *Waves and Stability in Continuous Media* (2008). DOI: 10.1142/9789812772350_0002.

[12] B. Detmann. "On Results of the Surface Wave Analyses in Poroelastic Media by Means of the Simple Mixture Model and the Biot Model". In: *Soil Dyn. Earthquake Eng.* 26.6-7 (2006), pp. 537–547. DOI: 10.1016/j.soildyn.2006.01.007.

[13] B. Detmann. "Propagation of Sound Waves in Partially Saturated Soils". In: *Proc. Appl. Math. Mech.* 8.1 (2008), pp. 10667–10668. DOI: 10.1002/pamm.200810667.

[14] M. T. van Genuchten. "A Closed-form Equation for Predicting the Hydraulic Conductivity of Unsaturated Soils". In: *Soil Sci. Soc. Am. J.* 44.5 (1980), pp. 892–898. DOI: 10.2136/sssaj1980.03615995004400050002x.

[15] P. Glover. *Fluid Saturation and Capillary Pressure*. May 2014. URL: http://homepages.see.leeds.ac.uk/~earpwjg/PG_EN/CD%20Contents/GGL-66565%20Petrophysics%20English/New%20Folder/Chapter%204.PDF.

[16] C. Görres and D. Chesmore. "Active Sound Production of Scarab Beetle Larvae Opens Up New Possibilities for Species-specific Pest Monitoring in Soils". In: *Sci. Rep.* 9.1 (2019). DOI: 10.1038/s41598-019-46121-y.

[17] H. F. Hemond and E. J. Fechner. "The Subsurface Environment". In: *Chemical Fate and Transport in the Environment*. Third. Elsevier Academic Press, 2015, pp. 219–310.

[18] Rodney Hill. "On Constitutive Macro-variables for Heterogeneous Solids at Finite Strain". In: *Proc. R. Soc. London, Ser. A* 326.1565 (1972), pp. 131–147. DOI: 10.1098/rspa.1972.0001.

[19] E. I. Inyang et al. "Subterranean Acoustic Activity Patterns of Vitacea Polistiformis (Lepidoptera: Sesiidae) in Relation to Abiotic and Biotic Factors". In: *Insects* 10.9 (2019), p. 267. DOI: 10.3390/insects10090267.

[20] C. S. Jog. "Balance Laws". In: *Continuum Mechanics: Foundations and Applications of Mechanics*. Cambridge University Press, 2015, pp. 166–202.

[21] S. N. Johnson et al. "Non-invasive Techniques for Investigating and Modelling Root-feeding Insects in Managed and Natural systems". In: *Agric. For. Entomol.* 9.1 (2007), pp. 39–46. DOI: 10.1111/j.1461-9563.2006.00315.x.

[22] M. B. Kirkham. "Water Movement in Saturated Soil". In: *Principles of Soil and Plant Water Relations* (2014), pp. 87–101. DOI: 10.1016/b978-0-12-420022-7.00007-0.

[23] R. W. Mankin, J. L. Brandhorst-Hubbard, and K. L. Flanders. "Acoustic Indicators for Mapping Infestation Probabilities of Soil Invertebrates". In: *J. Econ. Entomol.* 100.3 (2007), pp. 790–800. DOI: 10.1093/jee/100.3.790.

[24] R. W. Mankin et al. "Eavesdropping on Insects Hidden in Soil and Interior Structures of Plants". In: *J. Econ. Entomol.* 93.4 (2000), pp. 1173–1182. DOI: 10.1603/0022-0493-93.4.1173.

[25] R. W. Mankin et al. "Methods for Acoustic Detection of Insect Pests in Soil". In: *Soil Sci. Soc. Am. J.* (Nov. 1998), pp. 3–8.

[26] R. W. Mankin et al. "Perspective and Promise: A Century of Insect Acoustic Detection and Monitoring". In: *American Entomologist* 57.1 (Jan. 2011), pp. 30–44. DOI: 10.1093/ae/57.1.30.

[27] P. B. Mcevoy. "Host Specificity and Biological Pest Control". In: *BioScience* 46.6 (1996), pp. 401–405. DOI: 10.2307/1312873.

[28] D. A. McQuarrie and J. D. Simon. *Molecular Thermodynamics*. University Science Books, 1999.

[29] A. Michelsen et al. "Plants as Transmission Channels for Insect Vibrational Songs". In: *Behavioral Ecology and Sociobiology* 11.4 (1982), pp. 269–281. DOI: 10.1007/bf00299304.

[30] M. L. Oelze, W. D. O'Brien, and RR. G. Darmody. "Measurement of Attenuation and Speed of Sound in Soils". In: *Soil Sci. Soc. Am. J.* 66.3 (2002), pp. 788–796. DOI: 10.2136/sssaj2002.7880.

[31] M. Ostoja-Starzewski et al. "Scaling to RVE in Random Media". In: *Adv. Appl. Math. Mech.* (2016), pp. 111–211. DOI: 10.1016/bs.aams.2016.07.001.

[32] W. R. Sanders et al. "Acoustic Detection of Arthropod Infestation of Grape Roots: Scouting for Grape Root Borer (Lepidoptera: Sesiidae)". In: *Florida Entomologist* 94.2 (2011), pp. 296–302. DOI: 10.1653/024.094.0224.

[33] J. E. Santos, J. M. Corberó, and J. Douglas. "Static and Dynamic Behavior of a Porous Solid Saturated by a Two-phase Fluid". In: *J. Acoust. Soc. Am.* 87.4 (1990), pp. 1428–1438. DOI: 10.1121/1.399439.

[34] D. R. Smitley. "European Chafer". In: *Handbook of Turfgrass Insect Pests*. Entomological Society of America, 2012, pp. 33–35.

[35] *Soil Types*. 2009. URL: https://www.rhs.org.uk/advice/profile?pid=179.

[36] C. Vincent et al. "Management of Agricultural Insects with Physical Control Methods". In: *Annual Review of Entomology* 48.1 (2003), pp. 261–281. DOI: 10.1146/annurev.ento.48.091801.112639.

[37] H. F. Wang. *Theory of Linear Poroelasticity: With Applications to Geomechanics and Hydrogeology*. Princeton University Press, 2000.

[38] J. E. White. *Underground Sound: Application of Seismic Waves*. Elsevier Academic Press, 1983.

[39] K. Wilmański. "Thermodynamical Admissibility of Biot's Model of Poroelastic Saturated Materials". In: *Arch. Mech.* 54 (2002), pp. 709–736.

[40] R. D. Wyckoff and H. G. Botset. "The Flow of Gas-Liquid Mixtures Through Unconsolidated Sands". In: *Physics* 7.9 (1936), pp. 325–345. DOI: 10.1063/1.1745402.

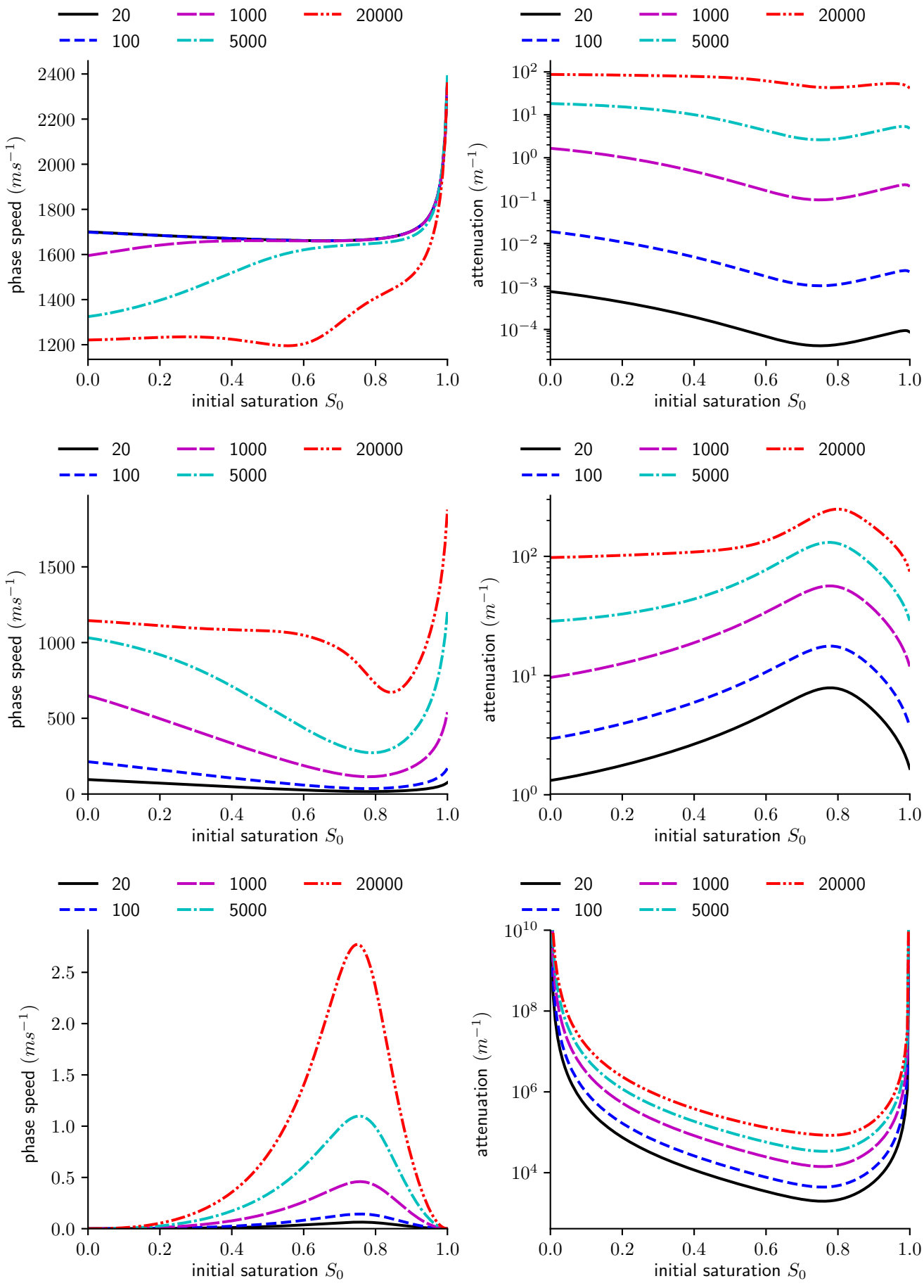

Figure 10: Plot against saturation